Current Research in Green and Sustainable Chemistry 4 (2021) 100116

Contents lists available at ScienceDirect

Current Research in Green and Sustainable Chemistry

journal homepage: www.elsevier.com/journals/current-research-in-green-and-sustainable-chemistry/2666-0865

Synthesis of mesoporous silica nanoparticles derived from rice husk and surface-controlled amine functionalization for efficient adsorption of methylene blue from aqueous solution

Leshan Usgodaarachchi [a], Charitha Thambiliyagodage [b,*], Ramanee Wijesekera [c], Martin G. Bakker [d]

[a] Department of Materials Engineering, Faculty of Engineering, Sri Lanka Institute of Information Technology, Malabe, Sri Lanka
[b] School of Science and Education, Faculty of Humanities and Sciences, Sri Lanka Institute of Information Technology, Malabe, Sri Lanka
[c] Department of Chemistry, Faculty of Science, University of Colombo, Colombo, 3, Sri Lanka
[d] Department of Chemistry and Biochemistry, The University of Alabama, Tuscaloosa, AL, 35387-0336, USA

ARTICLE INFO

Keywords:
Mesoporous silica nanoparticles
Functionalization
APTES
Rice husk
Methylene blue

ABSTRACT

Mesoporous silica nanoparticles (MSN) were synthesized using rice husk (RH) as the raw material via sol-gel pathway using cetyltrimethylammonium bromide (CTAB) as the structure directing agent. Silica nanoparticles were successfully functionalized with 3-aminopropyl triethoxysilane (APTES) via in-situ and post functionalization methods. Synthesized nanoparticles were characterized by X-Ray diffraction spectroscopy (XRD), scanning electron microscopy (SEM), fourier-transform infrared spectroscopy (FT-IR), thermogravimetric analysis (TGA) and Brunauer-Emmett-Teller (BET) surface area analysis. The amorphous silica nanoparticles were of 50–60 nm in diameter with a surface area of 150 m^2/g, pore volume of 0.237 cm^3/g and average pore size of 3.62 nm. Morphology and textural parameters were changed upon functionalization. The equilibrium adsorption capacity of MSN-A (4.94 mg/g) to adsorb 10 mg/L methylene blue (MB), was higher than in amine functionalized silica nanoparticles. The influence of experimental factors such as pH, adsorbent dosage, and initial MB concentration on adsorption of MB to MSN-A were studied. The equilibrium data for MB adsorption on mesoporous silica nanoparticles well fitted to Langmuir equation, with a maximum monolayer capacity of 19.26 mg/g. The adsorption of MB could be best described by the pseudo-second order model. The results indicate that MSN-A is a potential mesoporous material fabricated by cheap natural resources to remove MB from aqueous solutions.

1. Introduction

In the middle of the 19th century, the second industrial revolution has led to the release of a large number of pollutants to the environment including heavy metals [1], pesticides [2], volatile organic compounds [3], and organic dyes [4]. These pollutants have critically impacted aquatic ecosystems as well as human health by causing allergies, skin cancer, neurological disorders, hypertension, cardiovascular diseases, and pulmonary diseases once absorbed through various pathways [5–7]. Dyes that are not readily biodegradable are released to water reservoirs by the runoffs from various industries such as textile, pharmaceutical, paper, plastic, food, pulp, etc. One of the main sources of dye waste is the textile industry. It has been estimated that over 10,000 different dyes and pigments are used industrially and over 7×10^5 tons of synthetic dyes are produced annually worldwide [8]. Up to 2×10^5 tons of different dyes are lost to effluents every year during the dyeing and finishing operations [9]. Worldwide, these dyes are subjected to conventional wastewater treatment processes. Many physical, chemical, and biological methods have been developed to reduce the pollutants in wastewater. Chemical methods such as coagulation/flocculation [10], Ion exchange [11], electrochemical processes [12], advanced oxidation processes [13] and biological methods including bacterial biodegradation [14], fungal biodegradation [15], and algal biodegradation [16] have been extensively used to remove organic dyes. However, these existing methods possess drawbacks such as low efficiency, low selectivity, and high cost. Adsorption is widely used by many researchers to remove pollutants in wastewater because of advantages such as low-cost, ease of operation and high stability and high utility of the adsorbents used [17]. Adsorption is

* Corresponding author.
E-mail address: charitha.t@sliit.lk (C. Thambiliyagodage).

https://doi.org/10.1016/j.crgsc.2021.100116
Received 12 March 2021; Received in revised form 20 May 2021; Accepted 22 May 2021
Available online 28 May 2021

an effective method to remove color from textile wastewater [18] using various low-cost adsorbents such as clays [19], zeolites [20], fly ash [21], activated carbon [22,23] and industrial waste products [24]. Among them activated carbon is the most effective adsorbent to remove organic dyes due to the large surface area and pore-volume, chemical inertness, and high mechanical stability of carbon [25,26]. However, the blockage of micropores of activated carbon by macro dye molecules makes it more difficult for large dye molecules to diffuse into the internal pore structure of activated carbon, limiting its applicability [27].

Mesoporous silica is a porous material that has been used as an absorbent due to its unique surface and pore properties such as high surface area and high pore volumes [28]. The first synthesis of structurally ordered Mobil Composition of Matter (MCM-type) mesoporous silica material was reported by scientists of Mobil Company in 1992 [29]. Unlike the inaccessible pores present in activated carbon, mesoporous silica has a pore structure appropriate for the adsorption of textile dye molecules. Naturally occurring silica especially that found in agricultural waste can provide an alternative source to expensive commercial silica precursors in the synthesis of mesoporous silica. Rice husk is the most utilized agriculture waste to be converted to more valuable silica derived end products [30]. Rice (*Oryza sativa*) which covers 1% of the earth's surface is a primary source of food for billions of people. Globally, approximately 600 million tons of rice are produced each year [31]. Rice husk, which is the coating of rice grains, is composed of 50% cellulose, 25–30% lignin, and 15–20% silica [32]. On average each kilogram of rice produced generates 0.28 kg of rice husk as the major waste product during milling. When the rice husk is burnt at a temperature above 500 °C, the organic components decompose and rice husk ash is obtained [33]. The SiO_2 present in rice husk ash has a purity of 94–96% with minor impurities like K_2O, Na_2O, and Fe_2O_3. The purity of SiO_2 obtained by incineration of rice husk can be further improved to 98–99%, if the rice husk is subjected to pretreatments like leaching in acids such as HCl, HNO_3, H_3PO_4 and H_2SO_4 which helps to remove the above mentioned impurities [33–35].

In this study we report the synthesis of mesoporous silica nanoparticles from rice husk ash and modification of the surface by 3-aminopropyl triethoxysilane (APTES) using three different pathways. Applicability of the produced silica nanoparticles to remove MB from artificial waste water is also studied in detail.

2. Experimental

2.1. Materials

The raw material, rice husk (RH) was obtained from a rice mill in the "Gampaha" district, Sri Lanka. All reagents used were of analytical grade, and their solutions were made using ultrapure water. Sulfuric acid (98%, H_2SO_4), hydrochloric acid (37% HCl), sodium hydroxide, 2-propanol, 3-aminopropyl triethoxysilane (APTES), toluene, dichloromethane, and diethyl ether were purchased from Sigma-Aldrich (USA). Methylene blue (MB) and cetyltrimethylammonium bromide (CTAB) were purchased from Sisco research laboratories (India).

2.2. Washing and acid treatment

Dirt, mud, and suspended soils in RH were removed by washing thoroughly with deionized water. The metallic impurities in RH were reduced to negligible levels by refluxing with 10% hydrochloric acid for 5 h at 80 °C. The solution was filtered and the husk was washed thoroughly with distilled water until the filtrate was free from acid. The RH was oven dried at 70 °C for 15 h.

2.3. Thermal treatment

The acid leached RH from 2.2 was burnt in a muffle furnace at 600 °C for 4 h to remove all the hydrocarbons. The product obtained is referred to as acid leached-RHA in the text hereafter.

2.4. Preparation of the silica precursor

RHA (10 g) was refluxed with 3.5 M sodium hydroxide at 80 °C for 5 h with vigorous stirring. The solution obtained was filtered through Whatman filter paper (no. 1) to obtain a colorless viscous solution. This solution was designated as Na_2SiO_3 stock solution.

2.5. Preparation of mesoporous silica nanoparticles (MSN-A)

Silica nanoparticles were prepared by the sol-gel technique. CTAB was dissolved in a solution of deionized water/2-propanol (1:1) to prepare a 2.0 wt % solution. Sodium silicate solution was added dropwise to the CTAB solution with stirring and stirring was continued for 15 min to obtain a homogeneous solution. Then 0.5 M sulfuric acid was added dropwise to initiate the hydrolysis-condensation reaction at 60 °C and the acid was added until the pH reached 4. The resulting gel mixture was aged at room temperature for 12 h. The aged silica gel was washed thoroughly with deionized water until free from sulfate anions. The washed gel was dried at 80 °C for 12 h. Finally, the obtained powder was well ground and calcined at 550 °C for 4 h. This sample is referred to as *MSN-A*.

2.6. Amine functionalization of silica nanoparticles

Surface modification of silica was carried out using two pathways: co-synthesis and post grafting methods using APTES as the surface modification reagent.

2.6.1. Amine modified MSN via co-synthesis method by pre addition of APTES (MSN-B)

APTES was added (Si: APTES molar ratio 1.2:1) after the addition of sodium silicate, while the rest of the procedure remained the same as in 2.5. This sample was referred to as *MSN-B*.

2.6.2. Amine modified MSN via co-synthesis method by post addition of APTES (MSN-C)

APTES was added (Si: APTES molar ratio 1.2:1) after the addition of 0.5 M sulfuric acid, while the rest of the procedure remained same as in 2.5. This sample was referred to as *MSN-C*.

2.6.3. Amine modified MSN via post grafting method (MSN-D)

Calcined MSN (1.0 g) and APTES (Si: APTES molar ratio 1.2:1) were refluxed in toluene (100 ml) at 120 °C for 6 h with vigorous stirring. The obtained sample was allowed to cool to room temperature and filtered through a Whatman no. 1 filter paper. The resulting sample was washed with a 1:1 mixture of dichloromethane and diethyl ether followed by drying in an oven at 80 °C. This sample was referred to as *MSN-D*.

2.7. Characterization of materials

The crystalline structure of MSN was examined by a Advance Bruker system X-ray diffractometer. The X-rays were generated at 30 mA current and 40 kV voltage equipped with a Cu target and CuKα ($\lambda = 0.15406$ nm) were selected. Samples were scanned in the range of diffraction angle (2θ) 3° to 90° at 2°/min scanning rate. The morphology and particle size of the silica nanoparticles were determined by Hitachi SU6600 FE-SEM (Field Emission Scanning Electron Microscope). FT-IR spectra of the MSN and the amine surface-modified nanoparticles were acquired in the range of 400–4000 cm^{-1} using an ATR device employing the ABB MB3000 FT-IR spectrophotometer. Thermogravimetric analysis (TGA) was performed using a TGA instrument SDT Q600 at a heating rate of 10 °C/min under nitrogen atmosphere. Nitrogen sorption isotherms were collected at 77 K using Quantachrome Autosorb IQ analyzer. Before the measurements, samples were evacuated for 10hr at 473 K.

2.8. Adsorption study

Batch studies were carried out where a known weight of the adsorbent was added to 50 ml of a known concentration of MB solution at a specific pH and shaken at 200 rpm in a Stuart orbital shaker at room temperature. The desired pH (in range of 2–14) of the dye solution was achieved via adjustment with 0.1 M HCl or 0.1 M NaOH solutions. Aliquots were withdrawn at pre-determined time intervals over 2 h. The concentration of MB was calculated by measuring absorbance at 665 nm using a Shimadzu UV-1900 spectrophotometer. The amount of MB adsorbed at time t (q_t) was calculated according to the following equation (1).

$$q_t = \frac{(C_0 - C_t)}{m} V \quad (1)$$

Where.

C_0 – Initial concentration of adsorbate (mg/L)
C_t – Concentration of adsorbate at time (min) t (mg/L)
m – Mass of adsorbent (g)
V – Volume of solution (L)

For the adsorption kinetics studies, the adsorbent dosage was varied (20–100 mg) and was kept in contact with a MB solution (10 mg/L) concentration at the optimized pH. The agitation speed was maintained at 200 rpm. The concentration at time t (C_t) and amount of MB adsorbed at time t (q_t) were determined by using the same procedure described above.

For the adsorption isotherm studies, the optimized weight of adsorbent was placed in contact with five different initial concentrations of MB solutions (5–25 mg/L) at the optimized pH. The agitation speed was kept at 200 rpm, and the concentration at equilibrium (C_e) and amount of MB adsorbed at equilibrium (q_e) was determined using the procedure given in 2.8.

3. Results & discussion

3.1. Textural properties and characteristics of the adsorbent materials

Unlike commercial silica, the RHA based silica is an agricultural waste product generated from RH. The RHA consists mainly of silica (>90%) and some metallic impurities such as Fe^{3+}, Ca^{2+}, Na^{+}, K^{+}, and Mg^{2+} which influence the purity and color of silica [36]. The minor metallic impurities could be eliminated by preliminary acid leaching treatments with hydrochloric, sulfuric, phosphoric or nitric acid before the combustion process [37]. The presence of metallic impurities during the combustion process results in crystalline silica and thus a considerable decrease in the surface area [38]. XRD patterns of RHA and Acid leached RHA are shown in Fig. 1.

XRD patterns of both RHA and Acid leached RHA are similar. The broad diffused peak with maximum intensity at $2\theta = 22^{\circ}$ indicates that only amorphous silica has been formed. Crystalline silica has not been formed because of the low calcined temperature used (600 °C). The combustion temperature has a critical influence on the crystallization of silica, which begins to occur above 900 °C [39]. Acid leaching has a considerable influence on the final color of silica (Fig. 2). RHA is light brown in colour while acid leached RHA is white. The color in RHA is due to the formation of metal oxides. Purity and the quality of RHA depend on various factors such as combustion temperature, combustion time, concentration of leaching acid solution, acid leaching time, and acid leaching temperature [35].

Mesoporous silica nanoparticles were obtained from sodium silicate solution via the sol-gel pathway. The surface area, pore size and pore volume of MSN depend on several factors such as type of surfactant, weight of surfactant, aging temperature, aging speed and aging time

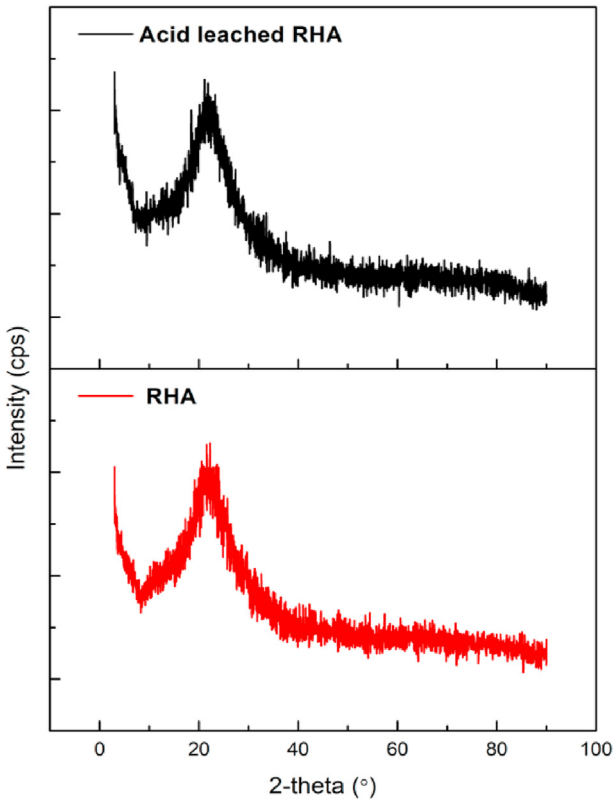

Fig. 1. XRD patterns of RHA and Acid leached RHA.

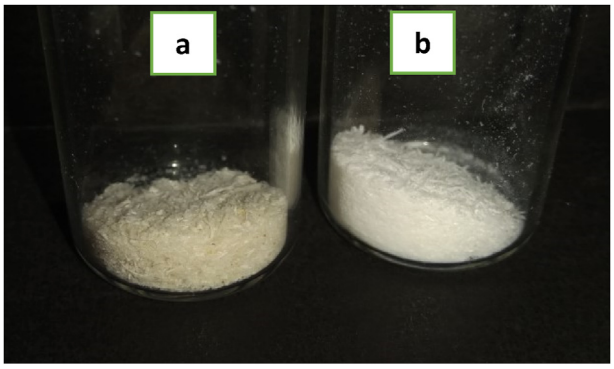

Fig. 2. (a) RHA (b) Acid leached RHA.

[35]. The surfactant plays a crucial role in the synthesis of mesoporous material via the sol-gel pathway. Surfactant concentration and length of the hydrophobic chain are critical parameters that determine the structure of the mesoporous material. CTAB is used as the surfactant in this study because it is composed of a cationic polar head and a hydrophobic tail that could aggregate negatively charged silica nanoparticles by both surface charge neutralization and hydrophobic effect [40]. The influence of CTAB in making porous structure of silica is shown in Fig. 3.

Sodium silicate stock solution was prepared by refluxing Acid leached RHA in 3.5 M NaOH. The balanced chemical reaction is expressed as follows.

$$SiO_2 + 2NaOH \rightarrow Na_2SiO_2 + H_2O$$

Silica nanoparticles were synthesized via sol-gel method by reacting sodium silicate, CTAB and 0.5 M H_2SO_4 acid, as follows.

$$Na_2SiO_3 + H_2SO_4 \rightarrow SiO_2 + Na_2SO_4 + H_2O$$

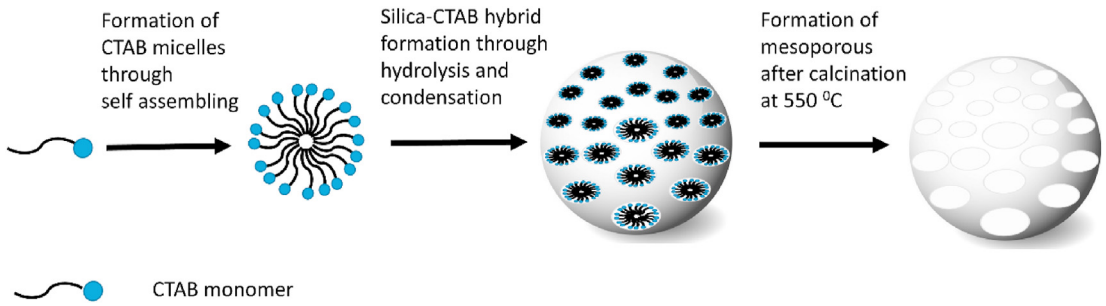

Fig. 3. The mechanism of formation of mesoporous silica spheres.

Complete precipitation of silica nanoparticles from sodium silicate solution occurs at pH 4. The acidity plays a very important role in the synthesis of silica nanoparticles. At a low silicate concentration and pH less than 8, $Si(OH)_4$ is the dominant species in aqueous solution. At higher concentrations the Si(OH) groups, spontaneously polymerize to yield higher oligomers linked by a disiloxy bond [41,42]. This type of reaction is most favorable when one of the silanols is deprotonated to give a $Si–O^-$ group. These oligomers grow into colloid sized silica particles as large particles grow at the expense of smaller ones [43].

To the selective functionalization of the inner and outer surface of mesoporous silica nanoparticles, aminopropyl functionalization was carried out in three different synthesis pathways based on post grafting and co-synthesis (in-situ) methods. The surface structure and morphology of MSN and aminopropyl functionalized silica were investigated using scanning electron microscopy. SEM image of the MSN-A (Fig. 4 (a)) shows roughly spherical nanoparticles of approximately about 50–60 nm. However, aminopropyl functionalized silica materials MSN-B, MSN-C and MSN-D In (Fig. 4 (b), 4 (c) and 4 (d), respectively) show different morphologies where most of the nanoparticles are aggregated, compared to the MSN-A.

FT-IR measurements were performed in order to identify the chemical functionality of the MSN-A and APTES functionalized silica nanoparticles and their FT-IR spectra are given Fig. 5. In general, silica exhibits Si–O stretching and bending vibration bands at the range of 400–1300 cm^{-1} [42]. The absorption bands at 1058 cm^{-1}, 803 cm^{-1}, and 457 cm^{-1} are assigned to Si–O–Si asymmetric stretching, Si–O–Si symmetric stretching and Si–O–Si bending vibration, respectively [44,45]. All three bands are found in MSN-A and amine functionalized materials. The adsorption band in the range of 3000–3800 cm^{-1} is prominent in MSN-A (Supplementary Fig. 1) and less prominent in other silica nanoparticles. This broad band is ascribed to O–H stretching of the silanol group (Si–OH) and physisorbed water [45,46]. The spectra indicate that no major changes to the silica framework have occurred upon functionalization from APTES. Fig. 5 (b) clearly shows the expanded vibration bands from 1400 to 1600 cm^{-1}. The IR vibration band with low intensity at 1479 cm^{-1} is assigned to CH_2 bending vibrations of functionalized silica materials [47]. The band at 1557 cm^{-1} in APTES functionalized samples could be assigned to the N–H bending vibration of the NH_2 group [48]. This band is more apparent in MSN-D.

Thermal degradation properties and stability of the surface functionalization reagent of the synthesized materials were studied using TG analysis. The TG analysis curves of MSN-A and amine-functionalized silica materials are shown in Fig. 6. Mesoporous silica nanoparticles are very stable throughout the analyzed temperature except in the initial temperature range. This instability is due to the presence of moisture in the mesopores framework. The presence of hydroxyl groups due to the adsorbed water by mesoporous silica was confirmed by FT-IR spectrum. Initial weight loss of 17.26, 4.75, 1.76 and 6.61% of MSN-A, MSN-B,

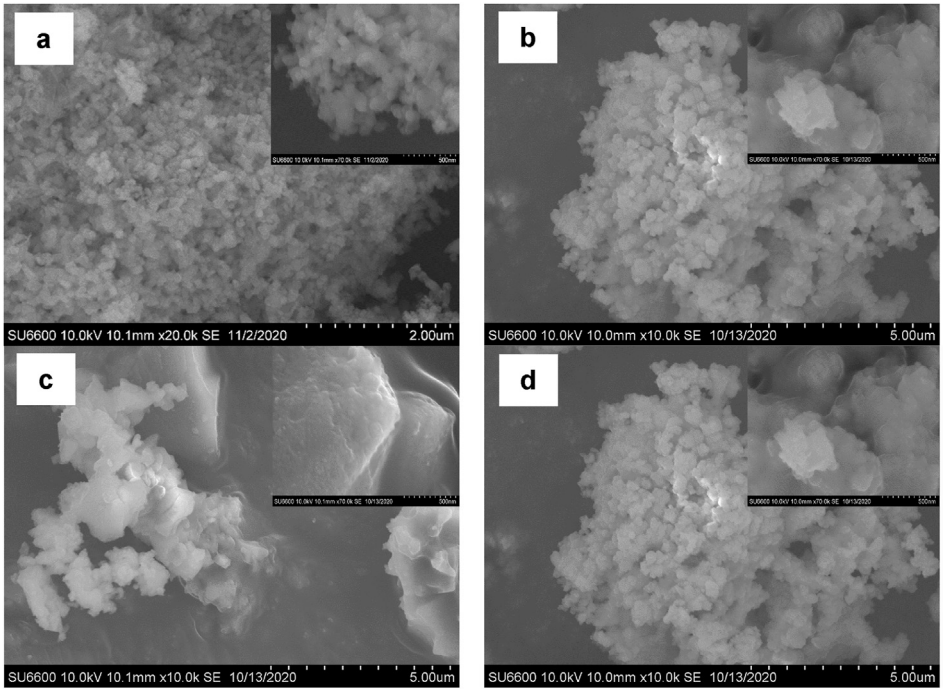

Fig. 4. SEM images of the (a) MSN-A, (b) MSN-B, (c) MSN-C and (d) MSN-D.

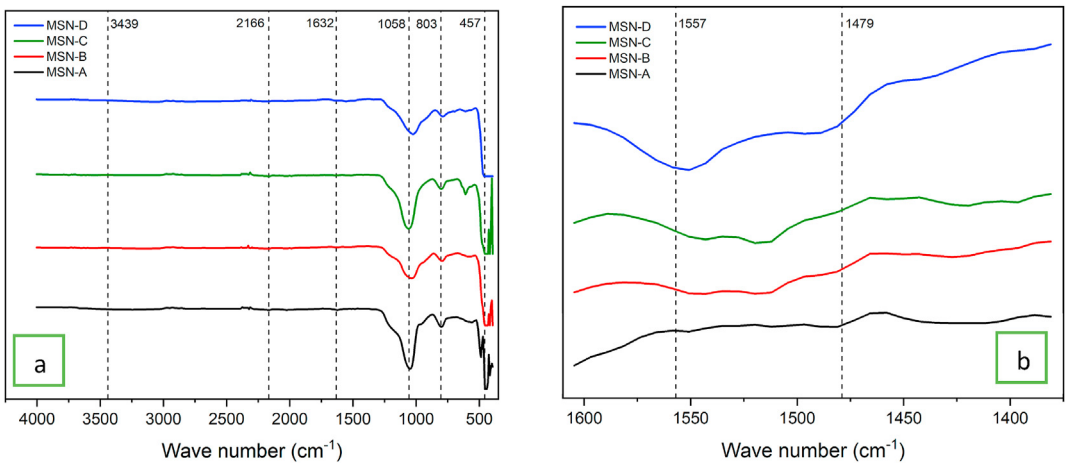

Fig. 5. (a) FTIR spectra of MSN-A and amine-modified silica particles, (b) FTIR spectra of MSN-A and amine-modified silica particles responsible for amine vibration bands.

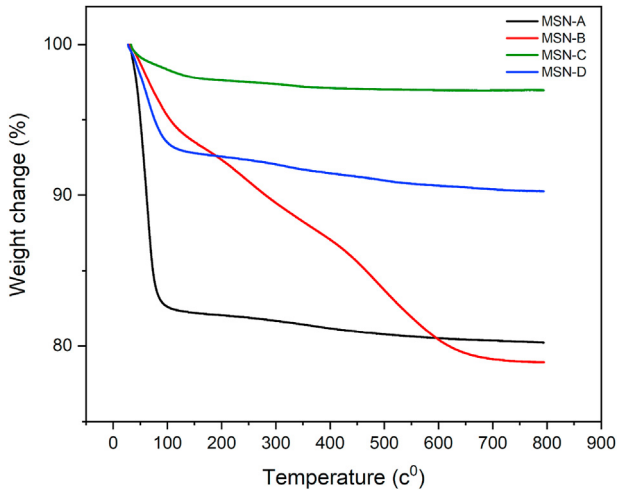

Fig. 6. TGA curves for MSN-A and amine-modified silica nanoparticles.

MSN-C and MSN-D, respectively in the initial temperature range is due to the loss of water. Slight weight loss observed in MSN-A, MSN-C and MSN-D in temperature range 100–800 °C was attributed to the surface dehydration and dihydroxylation of the silica structure [49].

However, the TG curve of the MSN-B material is quite different to the others where a gradual weight loss was seen in this temperature range. This behavior could be due to the continuous surface dehydration, dihydroxylation and condensation of the grafted aminopropyl groups [49,50].

The adsorption isotherm is important for determining the behavior of an adsorbent. The specific surface area was calculated using Burnauer-Emmett-Teller (BET) theory. Total pore volume was determined from the amount of nitrogen adsorbed at a relative pressure of 0.99. The external surface area was calculated from the linear multi point BET plot. Pore size distribution was obtained from the desorption branch of Barrett-Joyner-Halenda (BJH) method. The specific surface area, pore volume and average pore diameters of MSN-A and amine functionalized silica are tabulated in Table 1.

The average pore diameters obtained for all the synthesized materials are in the range of 2–50 nm, confirming that the porous system consists mainly of mesopores. MSN-D showed the highest BET surface area, pore size and pore volume due to the migration of bulky APTES molecules into the pore structure of silica nanoparticles [51,52]. However, to clearly distinguish the effective functionalization method of the co-synthesis

Table 1
Textural parameters of MSN-A and functionalized silica materials.

Sample	Surface area S_{BET} (m^2g^{-1})	Average pore size (nm)	Pore Volume, V_{pore} (cm^3g^{-1})
MSN-A	150.28	3.62	0.24
MSN-B	31.65	3.15	0.05
MSN-C	30.98	2.66	0.04
MSN-D	222.51	19.30	0.27

pathway, APTES was introduced to the reaction mixture prior to and after the synthesis of silica nanoparticles. The results indicated that both MSN-B and MSN-C have similar BET surface areas suggesting that addition of APTES prior to or after synthesis of silica nanoparticles does not affect their surface area. The BET isotherm equation is given below in equation (2). The constant c in equation (2) represents the idea of degree of interaction between adsorbent and adsorbate.

$$\frac{p}{n(p^0-p)} = \frac{c-1}{n_m c}\left(\frac{p}{p^0}\right) + \frac{1}{n_m c} \quad (2)$$

In this work, the c values obtained from the BET analysis for MSN-A, MSN-B, MSN-C and MSN-D were 25.311, 1.969, 3.792 and 1.716 respectively. The value of c for MSN-A is relatively higher compared to that of amine functionalized materials indicating its stronger gas adsorption nature. Also, kinetics study MSN-A shows excellent adsorption capacity for adsorption of methylene blue than amine functionalized materials due to the strong interaction between adsorbent and adsorbate.

The nitrogen adsorption-desorption isotherms and pore size distribution curves of MSN-A and amine functionalized silica materials are shown in Fig. 7. MSN-A exhibits a type (iv) isotherm with H1 hysteresis loop as defined by IUPAC. Three well defined stages of isotherm shapes were clearly recognized as follows. The first region around $P/P_0 = 0.1$ is due to the gradual increase in nitrogen uptake at low relative pressure corresponding to monolayer adsorption on mesoporous pore walls, the second region appeared in the P/P_0, 0.1 to 0.9 range due to the capillary condensation within the mesoporous framework and, the third region at high P/P_0 (above 0.9) is attributed to the multilayer adsorption on the external surface of the material [51,53]. However, the amine-functionalized materials show type (III) isotherms due to the relatively weak interactions between the adsorbent and adsorbate. Fig. 7 (b) shows BJH pore size distribution curves of MSN-A and amine functionalized materials. The average pore size of MSN-D is greater than that of others, and the pore size distribution curve consists of multiple peaks suggesting that the pore distribution is non-uniform. However, the presence of narrow peaks in the mesoporous range (2–50 nm) indicate

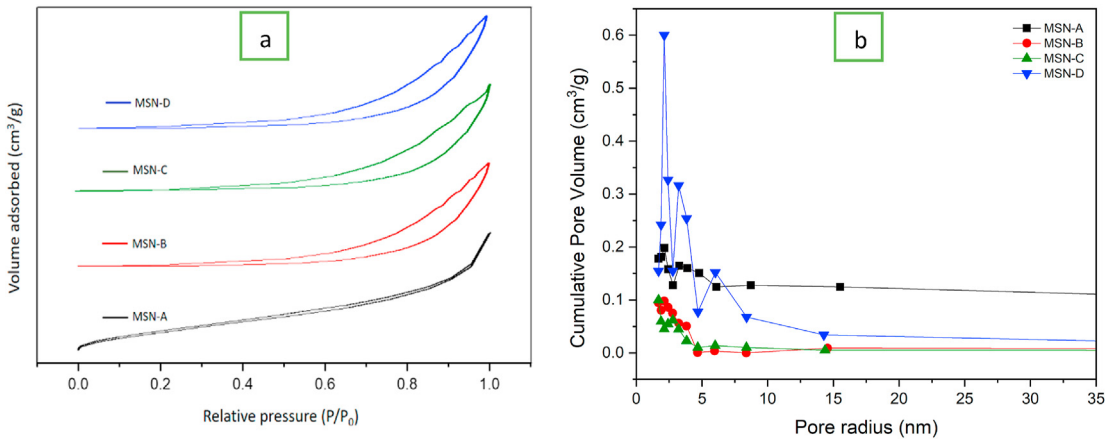

Fig. 7. (a) Nitrogen adsorption-desorption isotherms of MSN-A and amine-modified silica nanoparticles. (b) Pore size distribution of MSN-A and amine-modified silica nanoparticles.

the presence of mesoporous channels. Further, MSN-D exhibits a less intense peak around 6 nm, resulting from the pore expanding effect of APTES during the post functionalization.

3.2. Adsorption studies

Methylene blue uptake by MSN-A and amine functionalized silica was investigated. Fig. 8 (a) shows the calibration plot of MB, absorbance vs concentration. The slope of calibration plot is 0.2051 with 0.99 linear regression correlation coefficient (r^2). The performance of the synthesized adsorbents is shown in Fig. 8 (b). Significant differences existed in the adsorption of MB before and after amine functionalization. It is observed that MSN-A shows excellent adsorption compared to the amine functionalized adsorbents under the studied conditions (i.e. 50 mg of adsorbent, 10 mg/L MB, pH 7).

The uptake of MB by all the adsorbents increased rapidly in the first 10 min and thereafter, increased gradually until the equilibrium was achieved at 60 min. The uptake achieved by MSN-A at the equilibrium (4.94 mg/g) is higher than for MSN-B (1.729 mg/g), MSN-C (0.482 mg/g) and MSN-D (0.236 mg/g) indicating that the negatively charged MSN shows a higher adsorption capacity than amine-functionalized silica materials. The presence of amino groups on functionalized materials yields a positive charge on the surface at pHs less than 9.8 (pKa of NH_3^+ group of APTES = 10.8) resulting in strong repulsions between the silica surface and the cationic MB, reducing the adsorption of MB. Further, as APTES is a large molecule, steric hindrance would limit the migration of MB molecules to the silica surface.

The removal of MB by adsorption depends mainly on the pH of the solution. When the electrostatic forces between the adsorbent surface and the adsorbate are strong, as in MSN-A, an increase in ionic strength will decrease the adsorption capacity [54]. Fig. 9 shows the influence of pH on the adsorption of MB to these adsorbents. MSN-A shows the highest adsorption capacity compared to the amine functionalized

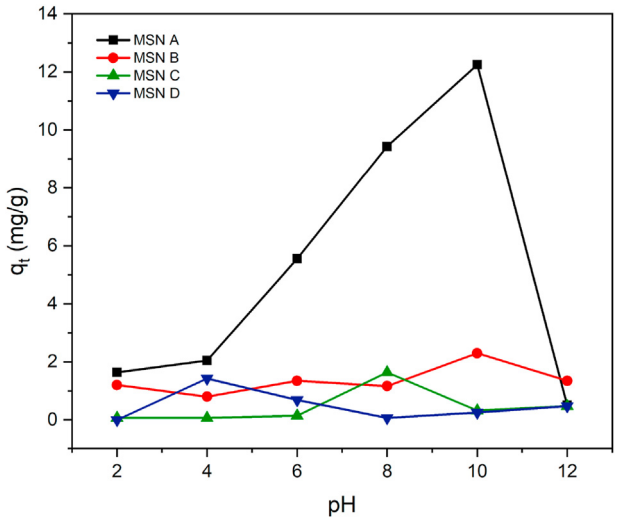

Fig. 9. Effect of pH on adsorption of MB on MSN-A, MSN-B, MSN-C and MSN-D adsorbents.

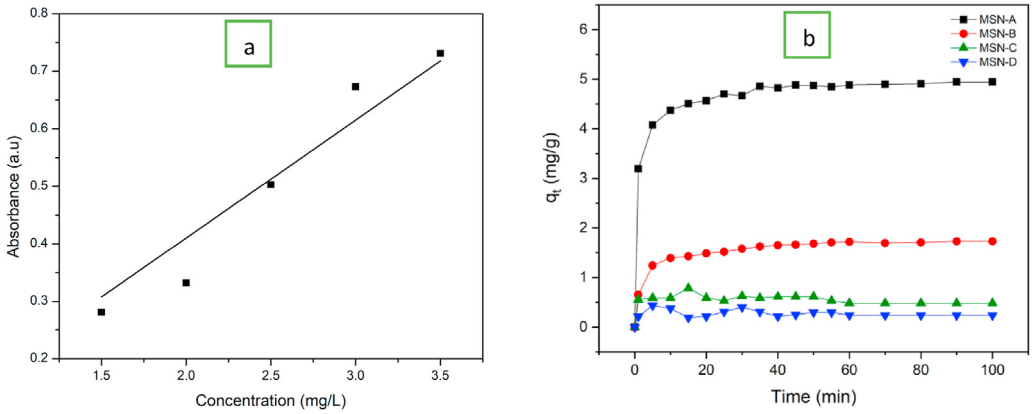

Fig. 8. (a) Calibration plot of MB and (b) Performance of MSN-A, MSN-B, MSN-C and MSN-D adsorbents on adsorption of MB.

adsorbents in the pH range 2–10. The lowest adsorption capacity of MSN-A was observed at pH 12 (0.511 mg/g), while the maximum (12.250 mg/g) was obtained at pH 10. The variation of adsorption capacity in the pH range (2-10) can be explained on the basis of electrostatic interactions between negatively charged MSN-A surface and cationic MB molecule. Low adsorption capacity at low pH values resulted as the negatively charged MSN-A surface is occupied by H^+ ions, limiting the surface available for MB adsorption. With increasing pH, as the concentration of H^+ decreases, the surface of MSN-A to becomes available to adsorb positively charged MB, resulting in high adsorption capacities. A shift of λ_{max} from 665 nm to 615 nm was observed at pH 12 due to the dimerization of MB [55]. A sudden drastic drop in the adsorption capacity was observed at pH 12. This is due to the inaccessibility of the dimerized molecules to the pore structure because of the steric hindrance.

Adsorbent dosage is an important parameter for evaluating the adsorption capacity of a material. Since MSN showed most effective adsorbent for MB, it was selected for further studies as reported below. Adsorbent dosage of MSN was varied in the range 0.02 g–0.1 g and the study was carried out at the optimum pH 10 and initial MB concentration of 10 mg/L. Fig. 10 shows the variation of percentage removal of MB with contact time for the different adsorbent dosages used.

According to Fig. 10, for all the adsorbent dosages used (20–100 mg), percentage dye removal increased sharply initially and thereafter increased gradually until the equilibrium was reached. The maximum percentage removal of approximately 74% was achieved by MSN-A dosages of 60–100 g. The adsorption capacities were calculated in order to understand the effect of adsorbent dosage on adsorption of MB. Fig. 11 shows the variation of adsorption capacities with adsorbent dosage. It was observed that the adsorption capacity at the equilibrium decreases with increasing adsorbent dosage. The highest adsorption capacity of 13.67 mg/g was achieved with 20 mg of MSN-A at pH 10.

Adsorption kinetics is essential to understand the rate of adsorbate uptake and the mechanism of the process. The applicability of the pseudo-first-order and pseudo-second-order models for the adsorption of methylene blue onto MSN-A were studied. The best-fit model was selected based on the linear regression correlation coefficient, and the r^2 values in adsorption kinetics models. A linear form of the pseudo-first-order model which was described by Lagergren et al. [56] is given in equation (3).

$$\ln(q_e - q_t) = ln\, q_e - k_1 t \tag{3}$$

Where.

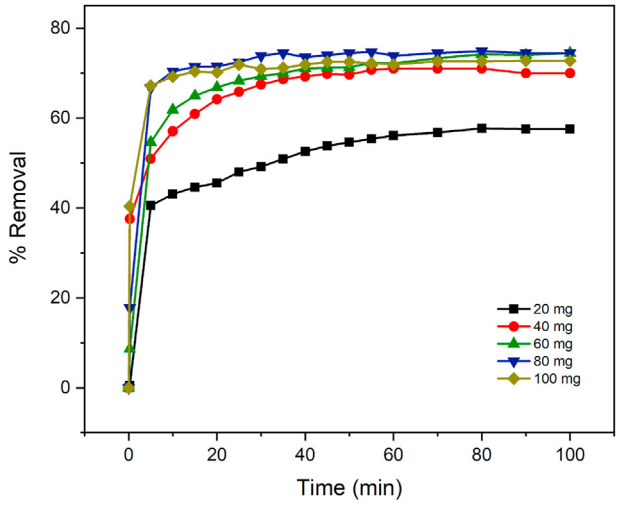

Fig. 10. The percentage removal of MB on different weight of MSN-A loading.

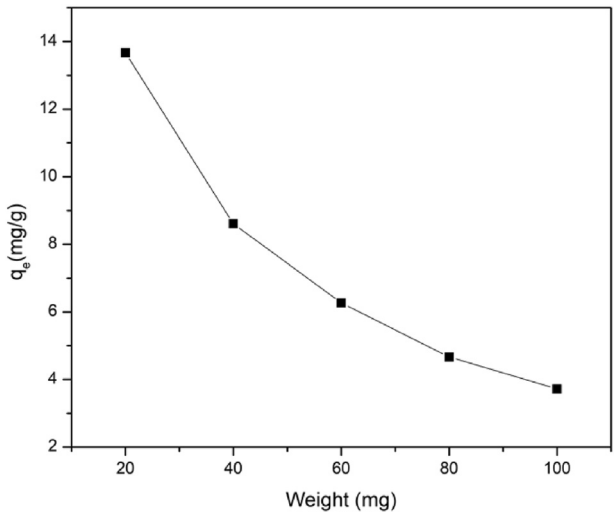

Fig. 11. Effect of MSN-A dosage on MB adsorption capacity.

q_e – Amount of adsorbed (adsorbate) at equilibrium per unit mass of adsorbent (mg/g)
q_t – Amount of adsorbed (adsorbate) at time t per unit mass of adsorbent (mg/g).
k_1 – Adsorption rate constant (1/min)
t – Time (min)

The values of $\ln(q_e - q_t)$ were calculated from the kinetic data obtained from the optimization of adsorbent dosage (Fig. 10). The calculated q_e values, first-order rate constants, and the corresponding linear regression correlation coefficients (r_1^2) are tabulated in Table 2. Fig. 12 (a) shows the pseudo-first-order kinetic model for adsorption of MB (10 mg/L) to MSN-A (at pH 10) with different adsorbent weights, at 298 K. According to the linear regression correlation coefficient values obtained data do not perfectly fit the pseudo-first order kinetic model. The highest r_1^2 (0.9616) value was obtained for 20 mg and r_1^2 values calculated for other adsorbent dosages showed a greater deviation from 1. Therefore, it can be concluded that the adsorption of MB to MSN-A does not follow the pseudo-first order kinetic model.

The linear formula for pseudo-second-order kinetics generally employed in the form proposed by Ho and McKay is shown in equation (4) [56].

$$\frac{t}{q_t} = \frac{1}{k_2 q_e^2} + \left(\frac{1}{q_e}\right) t \tag{4}$$

Where.

q_e – Amount of adsorbed (adsorbate) at equilibrium per unit mass of adsorbent (mg/g)
q_t – Amount of adsorbed (adsorbate) at time t per unit mass of adsorbent (mg/g)
k_2 – Adsorption rate constant (g/min * mg)

The values of $\frac{t}{q_t}$ were calculated from the kinetic data obtained from the optimization of adsorbent dosage. The calculated q_e values, the second-order rate constant values, and the corresponding linear regression correlation coefficients (r_2^2) are summarized in Table 2. Fig. 12 (b) shows the pseudo-second-order kinetic model for adsorption of MB (10 mg/L) to MSN-A (at pH 10), with different adsorbent dosages, at 298 K.

Above linear pseudo-second-order kinetic model plots of $\frac{t}{q_t}$ vs t show good agreement between experimental $q_{e,exp}$, and calculated q_e values. The correlation coefficients (r_2^2) of all the adsorbent dosages for the pseudo-second-order kinetics model are greater than 0.99. Therefore, it is

Table 2
Kinetic parameters for adsorption of methylene blue to MSN-A.

Adsorbent weight (mg)	$q_{e,\ exp}$ (mg g^{-1})	Pseudo-first order model			Pseudo-second order model		
		q_e (mg g^{-1})	k_1 (min^{-1})	r_1^2	q_e (mg g^{-1})	k_2 (g mg^{-1} min^{-1})	r_1^2
20	13.6762	8.4007	0.0522	0.96162	14.4801	0.0122	0.99866
40	8.7396	4.7698	0.0783	0.93884	8.9102	0.0520	0.99943
60	6.2774	2.2649	0.0490	0.89670	6.4416	0.0570	0.99981
80	4.6646	1.5749	0.1153	0.90330	4.7054	0.3247	0.99996
100	3.7097	0.5455	0.0648	0.66912	3.7344	0.4110	0.99995

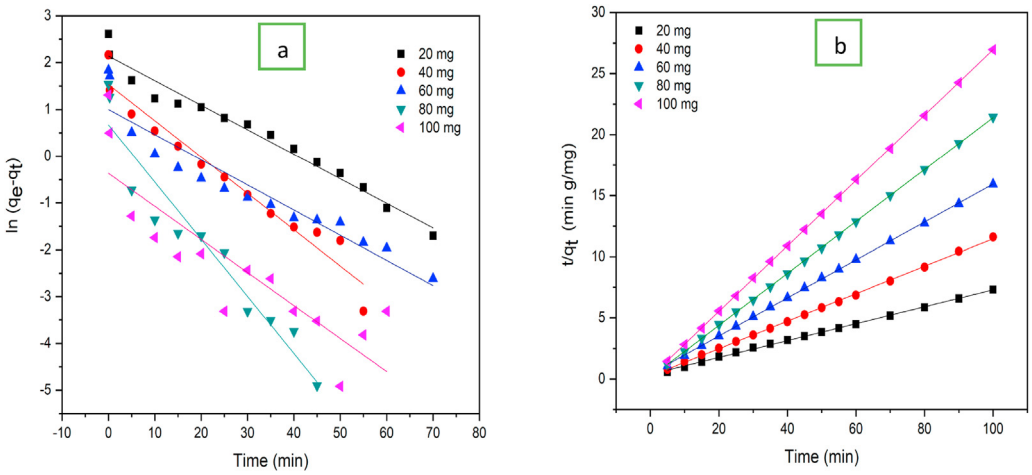

Fig. 12. (a) Pseudo-first-order and (b) Pseudo-second-order kinetics model for adsorption of MB to MSN-A.

evident that the adsorption of MB to MSN-A follows pseudo - second order kinetic model.

The adsorption isotherms in this study describe how MB molecules interact with the MSN-A adsorbent. The relationship between q_e and C_e can generally fit into many isotherm models. Among them, Langmuir, Freundlich, and Temkin isotherm models were selected for this study.

Langmuir adsorption isotherm was originally developed to describe gas–solid-phase adsorption onto activated carbon. In its formulation, this empirical model assumes monolayer adsorption onto a surface containing a finite number of definite localized sites. The model assumes uniform energies of adsorption onto the surface with no lateral interaction and steric hindrance between the adsorbed molecules, even on adjacent sites [57]. The linearized Langmuir equation can be written in the following form (equation (5)).

$$\frac{C_e}{q_e} = \frac{1}{q_m K_L} + \frac{C_e}{q_m} \tag{5}$$

Where.

C_e – Equilibrium concentration of the adsorbate (mg/L)
q_e - Amount of adsorbed (adsorbate) at equilibrium per unit mass of adsorbent (mg/g)
K_L - Langmuir constant related to adsorption capacity (L/mg)
q_m - Practical limiting adsorption capacity (mg/g)

The values of q_m and K_L were calculated from the slope and the intercept of the straight lines of the plot $\frac{C_e}{q_e}$ vs. C_e. Fig. 13 (a) shows the Langmuir adsorption isotherm model.

The Freundlich isotherm applies to adsorption processes that occur on heterogonous surfaces and describes the non-ideal reversible adsorption process [58]. The linear form of the Freundlich isotherm model can be written as in equation (6).

$$\log q_e = \log K_F + \frac{1}{n} \log C_e \tag{6}$$

Where.

q_e - Amount of adsorbed (adsorbate) at equilibrium per unit mass of adsorbent (mg/g)
C_e – Equilibrium concentration of the adsorbate (mg/L)
K_F – Freundlich adsorption capacity (mg/g)
1/n – Adsorption intensity

The values of n and K_F were calculated from the slope and the intercept of the straight lines of the plot $\log q_e$ vs. $\log C_e$, respectively. Fig. 13 (b) shows the Freundlich adsorption isotherm model.

The Temkin isotherm model considers the effects of indirect adsorbate/adsorbent interactions on the adsorption process, by ignoring the extremely low and large value of concentrations [59]. This model assumes that the heat of adsorption of all molecules in the layer would decrease linearly as a result of increase in surface coverage [60]. The linear form of the Temkin isotherm model can be written in the following form (equation (7)).

$$q_e = \frac{RT}{b} \ln K_T + \frac{RT}{b} \ln C_e \tag{7}$$

Where.

q_e - Amount of adsorbed (adsorbate) at equilibrium per unit mass of adsorbent (mg/g)
C_e - Equilibrium concentration of the adsorbate (mg/L)
R -Universal gas constant (J $mol^{-1}K^{-1}$)
T - Absolute temperature (K)
K_T - Temkin isotherm constant (L g^{-1})
b - Temkin constant which related to heat (J mol^{-1})

The values of b and K_T were calculated from the slope and intercept of the straight lines of the plot q_e vs. $\ln C_e$. Fig. 13 (c) shows the Temkin adsorption isotherm model.

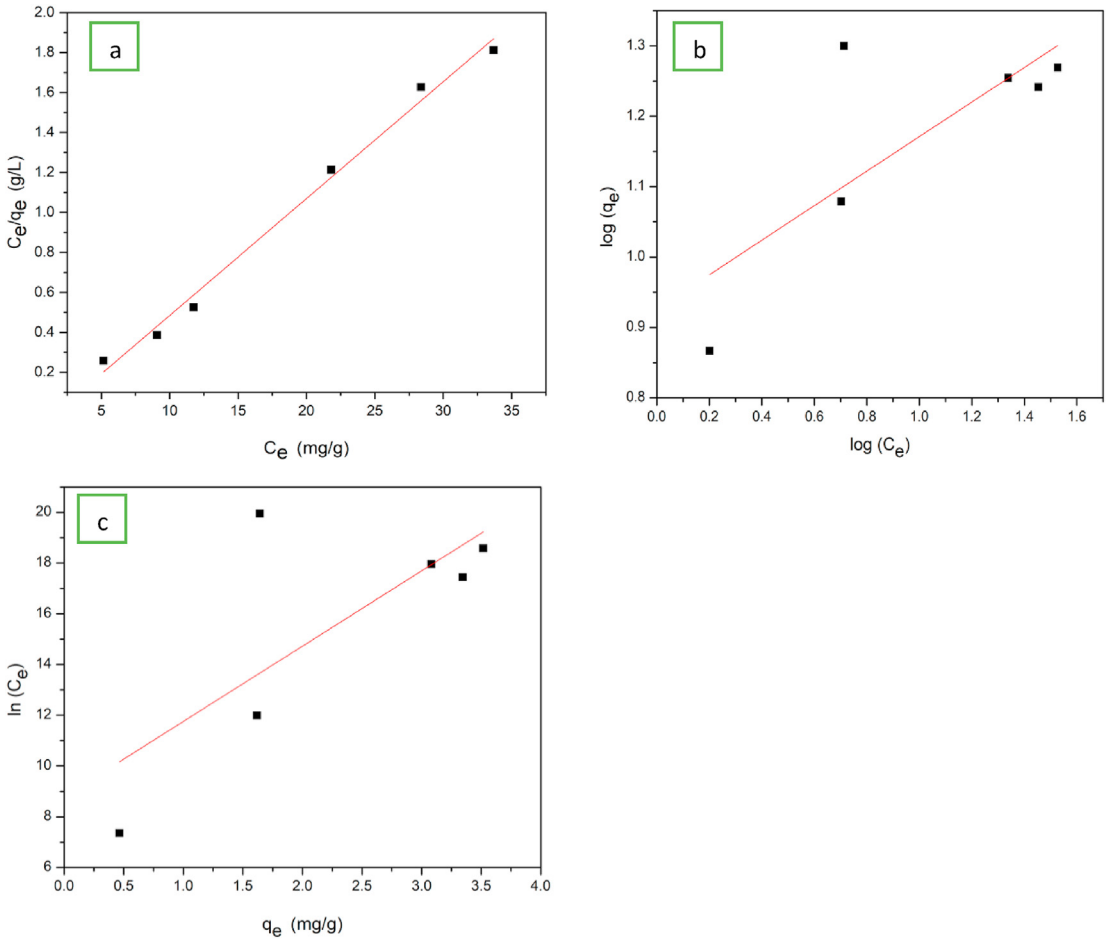

Fig. 13. (a) Langmuir, (b) Freundlich and (c) Temkin adsorption isotherm models of MB adsorption onto MSN-A.

The adsorption isotherms were obtained for different MB concentrations (15, 20, 25, 30, 35, and 40 mg/L) at pH 10, using 20 mg of MSN-A, at 298 K. The values of q_m, K_L, K_F, n, K_T, b along with the correlation coefficients (r^2) are summarized in Table 3.

The best fit with a correlation coefficient of 0.9898 was obtained for the Langmuir adsorption isotherm model suggesting that the adsorption of MB to MSN-A follows Langmuir adsorption. The maximum adsorption capacity of MSN-A calculated by data obtained from Langmuir model is 19.267 mg/g at 298 K.

Webber and Chakkravorti modified the Langmuir equation in 1974 by introducing a dimensionless constant they called the separation factor (R_L) [61]. The separation factor can be expressed as given in equation (8).

$$R_L = \frac{1}{1 + K_L C_0} \tag{8}$$

Where.

K_L - Langmuir constant (L/mg)
C_0 - Initial concentration of adsorbate (mg/L)

In explanation, R_L value indicates the adsorption nature to be either unfavorable ($R_L > 1$), linear ($R_L = 1$), favorable ($0 < R_L < 1$) or irreversible ($R_L = 0$).

The obtained R_L value of Langmuir adsorption varies from 0.0048 to 0.2728 and indicates that the adsorption of methylene blue to MSN-A is favorable.

The reusability of the adsorbent was assessed by performing multiple adsorption-desorption cycles. Adsorption of methylene blue was carried out for 10 ppm of MB (50 ml) at pH 10, using 0.02 g/l of MSN-A for 120 min. After each cycle MSN-A was washed with ethanol until a transparent solution was obtained. The C/C_0 vs time and equilibrium adsorption capacities for five cycles are shown in Fig. 14 (a) and (b), respectively.

As shown in Fig. 14 (a) the adsorption rate of MB to MSN-A decreased moving from the first cycle to the fifth cycle. The equilibrium adsorption capacity decreased from 13.72 at the first cycle to 11.05 mg/g at the fifth cycle as shown in Fig. 14 (b).

The percentage drop in equilibrium adsorption capacities were calculated and it was found that there is only 2.2% drop at the second cycle but at the fifth 19.5% drop in the equilibrium adsorption capacity was obtained. The reduction of adsorption capacities could have resulted due to the blocking of mesopores by the chemisorbed bulky MB molecules following in a reduction of the surface area.

Table 3
Parameters calculated by Langmuir, Freundlich and Temkin adsorption isotherm models.

Temperature (K)	Langmuir			Freundlich			Temkin		
	q_m	K_L	r^2	K_F	n	r^2	K_T	b	r^2
298	19.2678	0.5330	0.9898	8.428	4.0749	0.5111	19.3103	834.724	0.4479

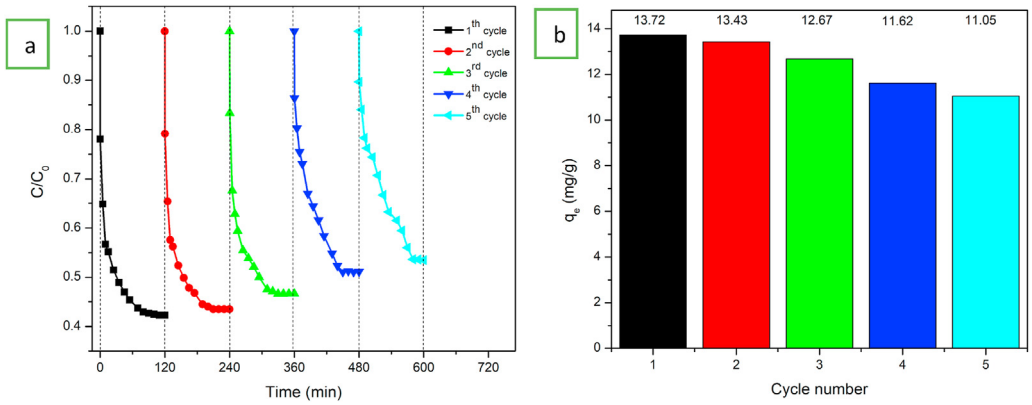

Fig. 14. (a) C/C_0 vs time (b) equilibrium adsorption capacity of five adsorption-desorption cycles.

4. Conclusions

Amorphous mesoporous silica nanoparticles of about 50–60 nm of high purity were synthesized from rice husk via the sol-gel pathway. Nanoparticles were successfully functionalized with APTES by in-situ and post functionalization methods. The point of addition of APTES during the functionalization of silica nanoparticles is important in determining the degree of functionalization. Pore expansion has taken place in the presence of APTES during the post functionalization. Presence of a negatively charged surface along with a considerable surface area and pore volume facilitate the adsorption of cationic methylene blue. Among the adsorbents tested, MSN-A showed the highest efficiency in removing MB where 95% of the removal was achieved in the first 30 min. The maximum efficiency was observed at pH 10. Adsorption of MB to MSN-A was best fitted to pseudo-second order kinetic model where MB molecules adsorb to MSN as a monolayer as revealed by Langmuir isotherm model. MSN-A exhibited excellent monolayer capacity of 19.26 mg/g at 298 K with 0.9898 linear regression correlation coefficient and 0.0048 to 0.2728 separation factor indicating better mathematical fit for the Langmuir adsorption model and favorable nature of adsorption of methylene blue to MSN.

Funding

This research was supported by the Accelerating Higher Education Expansion and Development (AHEAD) Operation of the Ministry of Higher Education funded by the World Bank.

CRediT authorship contribution statement

Leshan Usgodaarachchi: Conceptualization, Data curation, Formal analysis, Investigation, Methodology, Writing – original draft. **Charitha Thambiliyagodage:** Conceptualization, Formal analysis, Funding acquisition, Project administration, Resources, Supervision, Writing – review & editing. **Ramanee Wijesekera:** Writing – review & editing, Funding acquisition, Resources. **Martin G. Bakker:** Writing – review & editing, Funding acquisition.

Declaration of competing interest

The authors declare that they have no known competing financial interests or personal relationships that could have appeared to influence the work reported in this paper.

Acknowledgments

Authors acknowledge Sri Lanka Institute of Nanotechnology for providing the instrument facilities.

Appendix A. Supplementary data

Supplementary data to this article can be found online at https://doi.org/10.1016/j.crgsc.2021.100116.

References

[1] J.G. Dean, F.L. Bosqui, K.H. Lanouette, Removing heavy metals from waste water, Environ. Sci. Technol. 6 (1972) 518–522, https://doi.org/10.1021/es60065a006.
[2] I. Mahmood, S.R. Imadi, K. Shazadi, A. Gul, K.R. Hakeem, Effects of pesticides on environment, in: Plant, Soil Microbes Vol. 1 Implic. Crop Sci., Springer International Publishing, 2016, pp. 253–269, https://doi.org/10.1007/978-3-319-27455-3_13.
[3] M.E. Jenkin, S.M. Saunders, M.J. Pilling, The tropospheric degradation of volatile organic compounds: a protocol for mechanism development, Atmos. Environ. 31 (1997) 81–104, https://doi.org/10.1016/S1352-2310(96)00105-7.
[4] X. Zhu, S. An, Y. Liu, J. Hu, H. Liu, C. Tian, S. Dai, X. Yang, H. Wang, C.W. Abney, S. Dai, Efficient removal of organic dye pollutants using covalent organic frameworks, AIChE J. 63 (2017) 3470–3478, https://doi.org/10.1002/aic.15699.
[5] H.M. Salem, A.A. Elfouly, Minerals reconnaissance at saint catherine area, southern central sinai, Egypt and their environmental impacts on human health, n.d. https://pdfs.semanticscholar.org/15c6/0db88ec07e40f721b3641483cccfbdaa2327.pdf. (Accessed 24 July 2020).
[6] G. Bringmann, R. Kühn, Comparison of the toxicity thresholds of water pollutants to bacteria, algae, and protozoa in the cell multiplication inhibition test, Water Res. 14 (1980) 231–241, https://doi.org/10.1016/0043-1354(80)90093-7.
[7] W. Guo, X. Liu, Z. Liu, G. Li, Pollution and potential ecological risk evaluation of heavy metals in the sediments around Dongjiang Harbor, Tianjin, in: Procedia Environ. Sci., Elsevier, 2010, pp. 729–736, https://doi.org/10.1016/j.proenv.2010.10.084.
[8] V.K. Gupta, R. Jain, A. Nayak, S. Agarwal, M. Shrivastava, Removal of the hazardous dye-Tartrazine by photodegradation on titanium dioxide surface, Mater. Sci. Eng. C 31 (2011) 1062–1067, https://doi.org/10.1016/j.msec.2011.03.006.
[9] H. Chaudhuri, S. Dash, A. Sarkar, Synthesis and use of SBA-15 adsorbent for dye-loaded wastewater treatment, J. Environ. Chem. Eng. 3 (2015) 2866–2874, https://doi.org/10.1016/j.jece.2015.10.009.
[10] S. Sadri Moghaddam, M.R. Alavi Moghaddam, M. Arami, Coagulation/flocculation process for dye removal using sludge from water treatment plant: optimization through response surface methodology, J. Hazard Mater. 175 (2010) 651–657, https://doi.org/10.1016/j.jhazmat.2009.10.058.
[11] S. Raghu, C. Ahmed Basha, Chemical or electrochemical techniques, followed by ion exchange, for recycle of textile dye wastewater, J. Hazard Mater. 149 (2007) 324–330, https://doi.org/10.1016/j.jhazmat.2007.03.087.
[12] C.A. Martínez-Huitle, E. Brillas, Decontamination of wastewaters containing synthetic organic dyes by electrochemical methods: a general review, Appl. Catal. B Environ. 87 (2009) 105–145, https://doi.org/10.1016/j.apcatb.2008.09.017.
[13] S.H.S. Chan, T.Y. Wu, J.C. Juan, C.Y. Teh, Recent developments of metal oxide semiconductors as photocatalysts in advanced oxidation processes (AOPs) for treatment of dye waste-water, J. Chem. Technol. Biotechnol. 86 (2011) 1130–1158, https://doi.org/10.1002/jctb.2636.
[14] A. Khalid, M. Arshad, D.E. Crowley, Biodegradation potential of pure and mixed bacterial cultures for removal of 4-nitroaniline from textile dye wastewater, Water Res. 43 (2009) 1110–1116, https://doi.org/10.1016/j.watres.2008.11.045.
[15] T.H. Kim, Y. Lee, J. Yang, B. Lee, C. Park, S. Kim, Decolorization of dye solutions by a membrane bioreactor (MBR) using white-rot fungi, Desalination 168 (2004) 287–293, https://doi.org/10.1016/j.desal.2004.07.011.
[16] N. Daneshvar, A.R. Khataee, M.H. Rasoulifard, M. Pourhassan, Biodegradation of dye solution containing Malachite Green: optimization of effective parameters using Taguchi method, J. Hazard Mater. 143 (2007) 214–219, https://doi.org/10.1016/j.jhazmat.2006.09.016.

[17] M. Ince, O. Kaplan İnce, An overview of adsorption technique for heavy metal removal from water/wastewater: a critical review, Int. J. Pure Appl. Sci. 3 (2017) 10–19, https://doi.org/10.29132/ijpas.358199.
[18] G. Crini, P.M. Badot, Application of chitosan, a natural aminopolysaccharide, for dye removal from aqueous solutions by adsorption processes using batch studies: a review of recent literature, Prog. Polym. Sci. 33 (2008) 399–447, https://doi.org/10.1016/j.progpolymsci.2007.11.001.
[19] A. Kausar, M. Iqbal, A. Javed, K. Aftab, Z.i.H. Nazli, H.N. Bhatti, S. Nouren, Dyes adsorption using clay and modified clay: a review, J. Mol. Liq. 256 (2018) 395–407, https://doi.org/10.1016/j.molliq.2018.02.034.
[20] B. Armağan, M. Turan, M.S. Çelik, Equilibrium studies on the adsorption of reactive azo dyes into zeolite, Desalination 170 (2004) 33–39, https://doi.org/10.1016/j.desal.2004.02.091.
[21] D. Sun, X. Zhang, Y. Wu, X. Liu, Adsorption of anionic dyes from aqueous solution on fly ash, J. Hazard Mater. 181 (2010) 335–342, https://doi.org/10.1016/j.jhazmat.2010.05.015.
[22] K.D. Belaid, S. Kacha, M. Kameche, Z. Derriche, Adsorption kinetics of some textile dyes onto granular activated carbon, J. Environ. Chem. Eng. 1 (2013) 496–503, https://doi.org/10.1016/j.jece.2013.05.003.
[23] M. Mitchell, W.R. Ernst, G.R. Lightsey, E.T. Rasmussen, P. Bagherzadeh, Adsorption of textile dyes by activated carbon produced from agricultural, municipal and industrial wastes, Bull. Environ. Contam. Toxicol. 19 (1978) 307–311, https://doi.org/10.1007/BF01685803.
[24] A.K. Jain, V.K. Gupta, A. Bhatnagar, Suhas, Utilization of industrial waste products as adsorbents for the removal of dyes, J. Hazard Mater. 101 (2003) 31–42, https://doi.org/10.1016/S0304-3894(03)00146-8.
[25] K.D. Belaid, S. Kacha, M. Kameche, Z. Derriche, Adsorption kinetics of some textile dyes onto granular activated carbon, J. Environ. Chem. Eng. 1 (2013) 496–503, https://doi.org/10.1016/j.jece.2013.05.003.
[26] X. Yuan, S.P. Zhuo, W. Xing, H.Y. Cui, X.D. Dai, X.M. Liu, Z.F. Yan, Aqueous dye adsorption on ordered mesoporous carbons, J. Colloid Interface Sci. 310 (2007) 83–89, https://doi.org/10.1016/j.jcis.2007.01.069.
[27] X. Zhuang, Y. Wan, C. Feng, Y. Shen, D. Zhao, Highly efficient adsorption of bulky dye molecules in wastewater on ordered mesoporous carbons, Chem. Mater. 21 (2009) 706–716, https://doi.org/10.1021/cm8028577.
[28] C.H. Huang, K.P. Chang, H. De Ou, Y.C. Chiang, C.F. Wang, Adsorption of cationic dyes onto mesoporous silica, Microporous Mesoporous Mater. 141 (2011) 102–109, https://doi.org/10.1016/j.micromeso.2010.11.002.
[29] C.T. Kresge, M.E. Leonowicz, W.J. Roth, J.C. Vartuli, J.S. Beck, Ordered mesoporous molecular sieves synthesized by a liquid-crystal template mechanism, Nature 359 (1992) 710–712, https://doi.org/10.1038/359710a0.
[30] R. Pode, Potential applications of rice husk ash waste from rice husk biomass power plant, Renew. Sustain. Energy Rev. 53 (2016) 1468–1485, https://doi.org/10.1016/j.rser.2015.09.051.
[31] M. Ozturk, N. Saba, V. Altay, R. Iqbal, K.R. Hakeem, M. Jawaid, F.H. Ibrahim, Biomass and bioenergy: an overview of the development potential in Turkey and Malaysia, Renew. Sustain. Energy Rev. 79 (2017) 1285–1302, https://doi.org/10.1016/j.rser.2017.05.111.
[32] M.S. Ismail, A.M. Waliuddin, Effect of rice husk ash on high strength concrete, Construct. Build. Mater. 10 (1996) 521–526, https://doi.org/10.1016/0950-0618(96)00010-4.
[33] P. Deshmukh, J. Bhatt, D. Peshwe, S. Pathak, Determination of silica activity index and XRD, SEM and EDS studies of amorphous SiO 2 extracted from rice Husk Ash, Trans. Indian Inst. Met. 65 (2012) 63–70, https://doi.org/10.1007/s12666-011-0071-z.
[34] Y. Zou, T. Yang, Rice husk, rice husk ash and their applications, in: Rice Bran Rice Bran Oil Chem. Process. Util, Elsevier, 2019, pp. 207–246, https://doi.org/10.1016/B978-0-12-812828-2.00009-3.
[35] V.H. Le, C.N.H. Thuc, H.H. Thuc, Synthesis of silica nanoparticles from Vietnamese rice husk by sol–gel method, Nanoscale Res. Lett. 8 (2013) 58, https://doi.org/10.1186/1556-276x-8-58.
[36] W. Xu, J. Wei, J. Chen, B. Zhang, P. Xu, J. Ren, Q. Yu, Comparative study of water-leaching and acid-leaching pretreatment on the thermal stability and reactivity of biomass silica for viability as a pozzolanic additive in cement, Materials 11 (2018), https://doi.org/10.3390/ma11091697.
[37] N. Yalçin, V. Sevinç, Studies on silica obtained from rice husk, Ceram. Int. 27 (2001) 219–224, https://doi.org/10.1016/S0272-8842(00)00068-7.
[38] E. Rafiee, S. Shahebrahimi, M. Feyzi, M. Shaterzadeh, Optimization of synthesis and characterization of nanosilica produced from rice husk (a common waste material), Int. Nano Lett. 2 (2012) 1–8, https://doi.org/10.1186/2228-5326-2-29.
[39] R.A. Bakar, R. Yahya, S.N. Gan, Production of high purity amorphous silica from rice husk, Procedia Chem 19 (2016) 189–195, https://doi.org/10.1016/j.proche.2016.03.092.
[40] E.Y. Bryleva, N.A. Vodolazkaya, N.O. Mchedlov-Petrossyan, L.V. Samokhina, N.A. Matveevskaya, A.V. Tolmachev, Interfacial properties of cetyltrimethylammonium-coated SiO2 nanoparticles in aqueous media as studied by using different indicator dyes, J. Colloid Interface Sci. 316 (2007) 712–722, https://doi.org/10.1016/j.jcis.2007.07.036.
[41] K.R. Andersson, L.S. Dent Glasser, D.N. Smith, Polymerization and Colloid Formation in Silicate Solutions, 1982, pp. 115–131, https://doi.org/10.1021/bk-1982-0194.ch008.
[42] E. Rafiee, S. Shahebrahimi, M. Feyzi, M. Shaterzadeh, Optimization of synthesis and characterization of nanosilica produced from rice husk (a common waste material), Int. Nano Lett. 2 (2012) 1–8, https://doi.org/10.1186/2228-5326-2-29.
[43] H.E. Bergna, Colloid Chemistry of Silica, 1994, pp. 1–47, https://doi.org/10.1021/ba-1994-0234.ch001.
[44] D. Battegazzore, S. Bocchini, J. Alongi, A. Frache, Rice husk as bio-source of silica: preparation and characterization of PLA-silica bio-composites, RSC Adv. 4 (2014) 54703–54712, https://doi.org/10.1039/c4ra05991c.
[45] C.J. Thambiliyagodage, V.Y. Cooray, I.N. Perera, R.D. Wijesekera, Eco-friendly porous carbon materials for wastewater treatment, in: Lect. Notes Civ. Eng, Springer, 2020, pp. 252–260, https://doi.org/10.1007/978-981-13-9749-3_23.
[46] K.S. Suslick, D.J. Flannigan, Inside a collapsing bubble: sonoluminescence and the conditions during cavitation, Annu. Rev. Phys. Chem. 59 (2008) 659–683, https://doi.org/10.1146/annurev.physchem.59.032607.093739.
[47] L. Ma, P. Luo, Y. He, L. Zhang, Y. Fan, Z. Jiang, Ultra-stable silica nanoparticles as nano-plugging additive for shale exploitation in harsh environments, Nanomaterials 9 (2019) 1683, https://doi.org/10.3390/nano9121683.
[48] D. Zhang, H.E. Hegab, Y. Lvov, L. Dale Snow, J. Palmer, Immobilization of cellulase on a silica gel substrate modified using a 3-APTES self-assembled monolayer, SpringerPlus 5 (2016) 48, https://doi.org/10.1186/s40064-016-1682-y.
[49] J.M. Kim, S.M. Chang, S.M. Kong, K.S. Kim, J. Kim, W.S. Kim, Control of hydroxyl group content in silica particle synthesized by the sol-precipitation process, Ceram. Int. 35 (2009) 1015–1019, https://doi.org/10.1016/j.ceramint.2008.04.011.
[50] M.V. Lombardo, M. Videla, A. Calvo, F.G. Requejo, G.J.A.A. Soler-Illia, Aminopropyl-modified mesoporous silica SBA-15 as recovery agents of Cu(II)-sulfate solutions: adsorption efficiency, functional stability and reusability aspects, J. Hazard Mater. 223–224 (2012) 53–62, https://doi.org/10.1016/j.jhazmat.2012.04.049.
[51] A.H. Karim, A.A. Jalil, S. Triwahyono, S.M. Sidik, N.H.N. Kamarudin, R. Jusoh, N.W.C. Jusoh, B.H. Hameed, Amino modified mesostructured silica nanoparticles for efficient adsorption of methylene blue, J. Colloid Interface Sci. 386 (2012) 307–314, https://doi.org/10.1016/j.jcis.2012.07.043.
[52] E. Vilarrasa-García, J.A. Cecilia, E.M.O. Moya, C.L. Cavalcante, D.C.S. Azevedo, E. Rodríguez-Castellón, "Low cost" pore expanded SBA-15 functionalized with amine groups applied to CO2 adsorption, Materials 8 (2015) 2495–2513, https://doi.org/10.3390/ma8052495.
[53] S. Kachbouri, N. Mnasri, E. Elaloui, Y. Moussaoui, Tuning particle morphology of mesoporous silica nanoparticles for adsorption of dyes from aqueous solution, J. Saudi Chem. Soc. 22 (2018) 405–415, https://doi.org/10.1016/j.jscs.2017.08.005.
[54] Y.S. Al-Degs, M.I. El-Barghouthi, A.H. El-Sheikh, G.M. Walker, Effect of solution pH, ionic strength, and temperature on adsorption behavior of reactive dyes on activated carbon, Dyes Pigments 77 (2008) 16–23, https://doi.org/10.1016/j.dyepig.2007.03.001.
[55] G.S. Singhal, E. Rabinowitch, Changes in the absorption spectrum of methylene blue with pH, J. Phys. Chem. 71 (1967) 3347–3349, https://doi.org/10.1021/j100869a039.
[56] Y.S. Ho, Review of second-order models for adsorption systems, J. Hazard Mater. 136 (2006) 681–689, https://doi.org/10.1016/j.jhazmat.2005.12.043.
[57] C.H. Chang, E.I. Franses, Adsorption dynamics of surfactants at the air/water interface: a critical review of mathematical models, data, and mechanisms, Colloids Surf. A Physicochem. Eng. Asp. 100 (1995) 1–45, https://doi.org/10.1016/0927-7757(94)03061-4.
[58] N. Ayawei, S.S. Angaye, D. Wankasi, E.D. Dikio, Synthesis, characterization and application of Mg/Al layered double hydroxide for the degradation of Congo red in aqueous solution, Open J. Phys. Chem. (2015) 56–70, https://doi.org/10.4236/ojpc.2015.53007, 05.
[59] N. Ayawei, A.N. Ebelegi, D. Wankasi, Modelling and interpretation of adsorption isotherms, J. Chem. (2017), https://doi.org/10.1155/2017/3039817.
[60] J.H. Lee, J.H. Kim, K. Choi, H.G. Kim, J.A. Park, S.H. Cho, S.W. Hong, J.H. Lee, J.H. Lee, S. Lee, S.Y. Lee, J.W. Choi, Investigation of the mechanism of chromium removal in (3-aminopropyl)trimethoxysilane functionalized mesoporous silica, Sci. Rep. 8 (2018) 1–11, https://doi.org/10.1038/s41598-018-29679-x.
[61] T.W. Weber, R.K. Chakravorti, Pore and solid diffusion models for fixed-bed adsorbers, AIChE J. 20 (1974) 228–238, https://doi.org/10.1002/aic.690200204.